Cold sprayed Cr-coating on Optimized ZIRLO™ claddings: the Cr/Zr interface and its microstructural and chemical evolution after autoclave

Journal of Nuclear Materials 560 (2022) 153505

Contents lists available at ScienceDirect

Journal of Nuclear Materials

journal homepage: www.elsevier.com/locate/jnucmat

Cold sprayed Cr-coating on Optimized ZIRLO^{TM} claddings: the Cr/Zr interface and its microstructural and chemical evolution after autoclave corrosion testing

Andrea Fazi*, Krystyna Stiller, Hans-Olof Andrén, Mattias Thuvander

Department of Physics, Chalmers University of Technology, Se-412 96 Gothenburg, Sweden

ARTICLE INFO

Article history:
Received 15 September 2021
Revised 29 November 2021
Accepted 31 December 2021
Available online 3 January 2022

Keywords:
Accident tolerant fuels
Atom Probe Tomography
Cr-coatings
Cold spray
Coated Zr claddings
Autoclave corrosion testing

ABSTRACT

Cr-coated Optimized ZIRLO^{TM} cladding material fabricated with the cold-spray deposition process is studied. Microstructure and chemistry of this material are investigated before and after exposure to autoclave corrosion testing with scanning electron microscopy, energy dispersive spectroscopy analysis, electron backscattered diffraction, transmission electron microscopy and atom probe tomography. The results are used to assess what changes have occurred upon autoclave exposure. The formation of a compact, 80 – 100 nm thick Cr_2O_3 layer is observed on the surface of the exposed samples. Nucleation of $ZrCr_2$ intermetallic phase is discovered at the Cr/Zr interface. This Laves phase nucleates inside the intermixed bonding layer that can be found in both pristine and exposed samples, and decorates the interface in the form of small particles (less than 50 nm in size). Using transmission electron microscopy and atom probe tomography the growth of a Zr-Cr-Fe phase was detected. This phase is found in the region of the Zr-substrate immediately adjacent to the coating, up to a few hundred nanometres distance from the Cr/Zr interface. A small degree of recrystallization occurs upon autoclave exposure in the 1-2 µm thick nanocrystalline layer produced on the Zr-substrate by the cold spray deposition method utilized for the fabrication of the Cr-coating.

1. Introduction

Cr-coated claddings have emerged as one of the best candidates for accident tolerant fuel (ATFs) for light water nuclear reactors (LWRs), particularly for applications in pressurised water reactors (PWRs) [1,2]. As a response to the Fukushima Daiichi nuclear accident in 2011, the ATF concept has appeared with the objective of providing nuclear fuels able to better withstand severe accident conditions. Cr-coatings would serve to protect the zirconium claddings from the severe and rapid oxidation that occurs when zirconium alloys are exposed to steam at elevated temperatures. This reaction results in the formation of H_2 gas, production of heat and deterioration of the claddings' mechanical properties, and it can be the cause of H_2 explosions [2]. Hence, being able to prevent or delay this phenomenon is deemed crucial for the success of ATFs. Better performances and longer fuel life are also expected advantages of the introduction of these new materials. Cr-coatings were selected for their ability to form a passivating chromia scale when exposed to water corrosion. Additionally, the relatively high hardness of pure metallic Cr is deemed able to protect the coated fuel from debris fretting [3], currently one of the main causes of fuel rod failure [4]. Cr-coatings can be deposited with different technologies, the main coating versions being currently developed are obtained with physical vapour deposition and cold spray deposition. Cold spray deposition is a thermal spray technology in which high pressure, hot gas is fed through a converging-diverging (de Laval) nozzle together with a powder. After the nozzle, the gas expands, accelerates and cools down, bringing the powder particles with it. The final achieved particle velocity can range between 300 m/s and 1200 m/s [5,6]. This jet of gas and particles is then directed onto the substrate surface. Here, the particles' impact on the surface will result in high-strain, high-rate plastic deformation. The severe plastic deformation is at the base of the coating formation process. In cold spray, the powder is not melted or partially melted during deposition and to achieve coating formation the particle velocity has to be above a certain threshold referred to as the critical velocity. Each powder/substrate system is characterized by a specific critical velocity, below this velocity the coating does not develop in thickness, while above it the process can start to erode the substrate as for grit blasting.

* Corresponding author.
E-mail address: fazi@chalmers.se (A. Fazi).

https://doi.org/10.1016/j.jnucmat.2022.153505

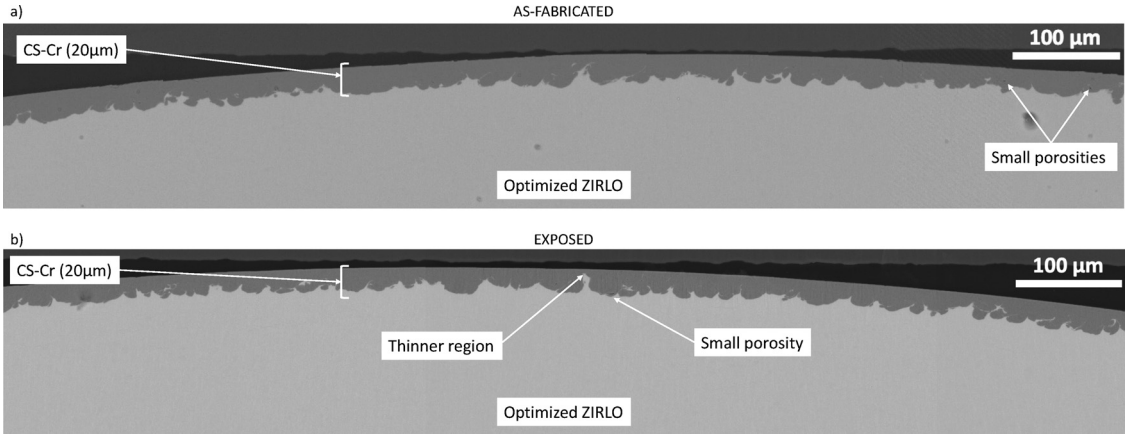

Fig. 1. Collage of multiple cross-sectional SEM images of as-fabricated (a) and autoclave exposed (b) CS-Cr-coated Optimized ZIRLO claddings.

Cr-coatings have demonstrated to perform well both in operating and severe accident conditions [7–12], the next step towards their commercial use requires the complete understanding of all chemical and microstructural changes the material undergoes during operation. The aim of this work is to investigate the corrosion protection offered by the Cr-coating; and to identify any active mechanisms that might be causing chemical or microstructural evolution of the material in the ranges of temperatures typical of operating conditions. To achieve this, as-fabricated and autoclave exposed materials are characterized and compared to each other in order to highlight changes in the microstructure due to autoclaving. A wide range of analysis methods are used for this scope, such as scanning electron microscopy (SEM), energy dispersive x-ray spectroscopy (EDS), transmission electron microscopy (TEM), electron backscattered diffraction (EBSD), and atom probe tomography (APT).

2. Experimental procedures

2.1. Material

Cold spray Cr-coated Optimized ZIRLO™ cladding material, in form of tubes 4 cm long and 10 mm in diameter, is analysed. Both as-fabricated samples, coated with 20 µm thick Cr-coating, and material exposed to autoclave corrosion testing are studied. The coating was obtained by depositing pure Cr feedstock powder sieved to less than 44 µm in size onto the Optimized ZIRLO alloy (OPZ) cladding tube (0.8-1.2 wt.% Nb, 0.6-0.79 wt.% Sn, 0.09-0.13 wt.% Fe, 0.09-0.16 wt.% O, balance Zr). The achieved particle velocity was 1200 m/s (+/- 50 m/s). The samples were first coated with 50 µm Cr, then the coating was ground down to 20 µm thickness. The exposure was performed in a closed loop, static, steam autoclave at 415°C and 220 bar for a total of 90 days in PWR water-chemistry. The standard temperature for static steam autoclave according to ASTM is 400°C [13], in this study the material was exposed at 415°C to test the material under slightly harsher conditions.

2.2. Sample preparation and analysis

A low-speed saw was used to cut the received samples into rings 5 mm in height. Bakelite embedded samples, ground and polished with SiC-paper and diamond particle suspensions, were subjected to SEM study and EDS analysis. Cross-sections prepared with broad ion beam (BIB) LEICA TIC3X were employed for EBSD mapping. APT and TEM specimens were extracted from the Bakelite-embedded samples with focused ion beam/scanning electron microscopy (FIB/SEM) in a dual-beam FEI Versa 3D workstation implementing well-known procedures for sample lift-out and preparation [14,15]. SEM and EDS analysis, conducted with a JEOL 7800F Prime microscope, provided an overview of the morphology and microstructure. EBSD mapping was performed on a TESCAN GAIA3 equipped with Oxford-NordlysNano detector and used to study microstructural changes happening during autoclave testing. TEM imaging was carried out on an FEI Tecnai T20 LaB_6 instrument and it allowed to identify the presence of small features at the Cr/Zr interface and to study the oxidation of the coating outer surface. An IMAGO LEAP 3000X HR was used to collect the APT data of the outer oxide and the Cr/Zr interface. All samples were run in laser mode with 200 kHz laser pulse frequency, at 50–70 K specimen temperature, 0.3 nJ laser pulse energy and 0.20 % evaporation rate. CAMECA IVAS 3.6.14 software was used for 3D reconstruction and data evaluation.

3. Results

An overview of the two coated cladding cross-sections analysed in this work is presented in Fig. 1. At this scale, it is difficult to see if any change occurred during autoclave exposure. The interface is rough and wavy, typical of cold sprayed coating/substrate interfaces. Small defects, as porosities and cracks, are present in the coating of both as-fabricated and exposed samples. Cold spray deposition can produce coatings with densities near 100%, but as it is possible to see in Fig. 1, some porosities are left after deposition, particularly in the regions between two former powder particles [16]. As these porosities are very few and isolated from the outer environment, they should not have any considerable effect on the oxidation protection offered by the coating. After coating deposition, the coating is ground from a thickness of 50 µm down to 20 µm. Due to the significant roughness of the Cr/Zr interface the coating can be significantly thinner in certain regions (see example in Fig. 1b), and there is the risk of exposing small portions of the bare substrate during the grinding process. This is not caused by the autoclave exposure or eventual dissolution of the coating. The combination of the intrinsic roughness of the cold sprayed coatings and the challenges involved in grinding a coating with precision is to blame for these coating defects. Still, the presence of the coating defect shown in Fig. 2b made it possible to investigate what would happen if the coating was damaged as a consequence of debris fretting or scratches. Fig. 2 shows two EDS maps taken from a cross-section of the autoclaved sample accompanied by the corresponding SEM images of the mapped region. In Fig. 2a a region representative of the general case is reported, here the coating is complete and the Zr substrate is fully protected (see

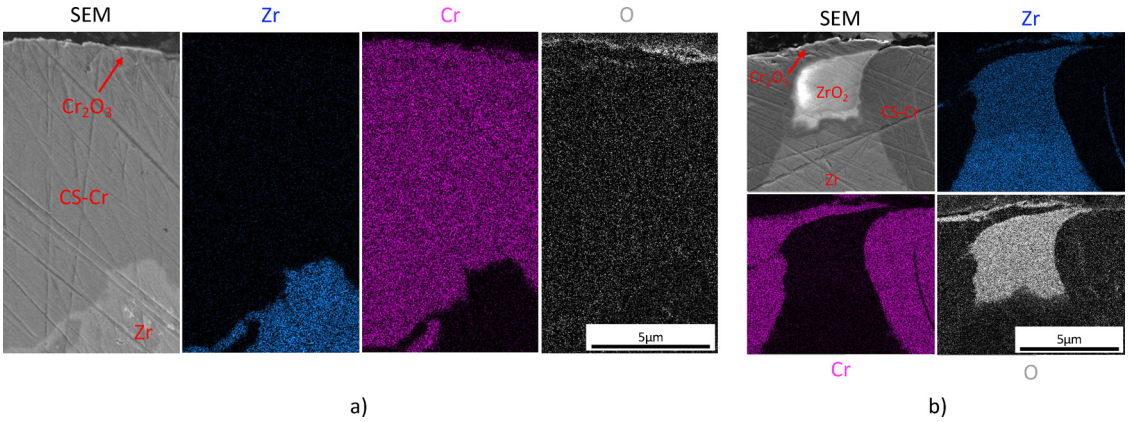

Fig. 2. EDS maps of CS-Cr coated Optimized ZIRLO cladding cross-section (zirconium signal in blue, chromium signal in magenta,oxygen signal in white). (a) Map over the outer diameter of the cladding in a region representative of general case. (b) Map over the outer diameter of the cladding in a region where a small portion of the Zr-substrate resulted exposed to the autoclave environment. (For interpretation of the references to colour in this figure legend, the reader is referred to the web version of this article.)

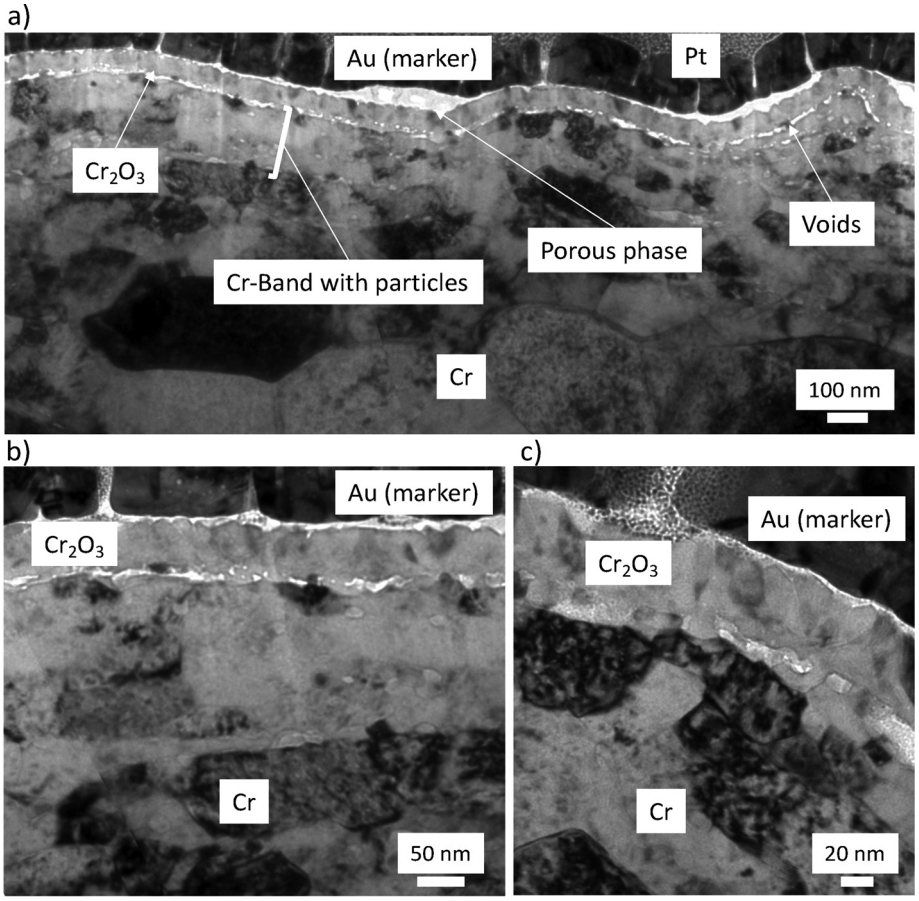

Fig. 3. BF-TEM imaging of oxide scale formed on the outer surface of the CS-Cr coating during autoclave exposure, low (a), medium (b) and high (c) magnification.

Zr and Cr maps). A thin layer of chromium oxide can be seen as a bright line in the SEM image and as a light-grey line in the O map. In Fig. 2b a specific region where the Zr is partially exposed is shown. Here, the chromium oxide is still present on top of the coating as expected, but some zirconium oxide is found growing inwards underneath the Cr-coating. The formation of ZrO_2 comes with volume expansion so that the oxide is locally pushing the Cr-coating outward, however no spallation of the coating is observed. The resulting exposure of the substrate has to be associated with the combination of the Cr/Zr interface roughness and the grinding of the coating surface that is performed after deposition, and it is not due to failure of the coating during exposure.

3.1. Oxidation behaviour of the Cr-coating

In the EDS maps shown in Fig. 2, the thin layer of chromium oxide that has formed on the outer surface of the Cr-coating after the autoclave exposure is visible. The thickness of this oxide is too thin to be assessed with use of SEM techniques. TEM imaging conducted on a lamella sample of the outermost surface of the coating is reported in Fig. 3 where the coating appears to be completely

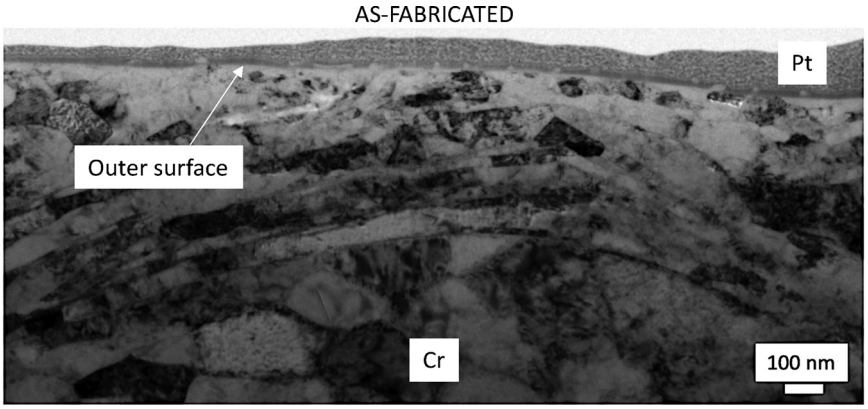

Fig. 4. BF-TEM images of the outer surface of the as-fabricated Cr-coating cladding.

covered by a 80-100 nm thick layer of chromium oxide. The thickness of the obtained chromia layer is comparable with the oxide developed by other Cr-coatings or chromia forming alloys tested under similar conditions (e.g. around 60 nm for PVD Cr-coating at 415°C for 100 days [17] and few hundreds of nm for Fe-Cr-Al alloys at 360°C for 1 year and 200 nm at 400°C for 72 h [18,19]). This layer is compact, adherent and homogeneous over the entire analysed surface. On top of the compact oxide, only in few regions, a porous and less compact phase can be found. Looking at Fig. 3a, it is possible to identify a band under the oxide (around 200 nm thick) where small particles or porosities appear distributed in the metallic Cr. Fig. 3b offers a better view of these features, but from the TEM it is difficult to define if they are porosities or particles. Nevertheless, it seems that they can be found everywhere distributed in this band. No sign of particles/porosities in the 200 nm region from the surface can be found for the as-fabricated material, as displayed in Fig. 4. Hence, the formation of these particles/porosities in the exposed material has to be linked to the autoclave corrosion testing.

To obtain the precise composition of the chromium oxide, APT runs including the oxide scale with the underlying metallic Cr were performed. One example of such measurements can be found in Fig. 5. Fig. 5a shows a 3D reconstruction of the APT data where the oxide/coating interface appears sharp with almost no interdiffusion, as shown in the proxigram [20] in Fig. 5b where the composition changes from pure chromium to around 60 at.% O and 40 at. % Cr in 5 nm or less. This value is extracted from the proxigram calculated from a 40 at.% O isosurface, using 0.10 nm steps and has to be taken as the maximum possible width of the interface. The software divides the dataset into a 3D grid with voxel size of 1 nm^3, in this case, and the difference between neighbouring voxels is smoothed using a delocalization algorithm [21], where the delocalization distances were $3\times3\times1.5$ nm^3. Undoubtedly, these processes can blur a perfectly sharp interface to a few nanometres. The measured composition of the oxide agrees with the composition of Cr_2O_3, suggesting that the oxide formed during autoclave exposure is chromia. Interestingly, small oxide particles could be found a few hundred nanometres below the coating surface. The presence of these small oxide particles was not ubiquitous and they could be measured only in some runs. Nevertheless, the distance of these oxide particles from the oxide scale would lead one to associate them with the particles/porosities that were visible in TEM, see Fig. 3. In Fig. 5 a and b, Fe (plotted as green dots in the 3D reconstruction) can be seen segregating at the Cr grain boundaries. Fig. 5 d shows a 1D concentration profile across one of the grain boundaries. Fe is present in small amounts as an impurity in the powder utilized for depositing the coating. In the as-fabricated material, ≈ 0.2 at.% Fe has been measured as uniformly distributed in the Cr-coating, but it appears to enrich grain boundaries when the material is exposed to autoclave testing. Other impurities measured with APT in the Cr coating comprise: ≈ 0.2 at.% C and ppm levels of Mn, Si and P.

3.2. Evolution of the Cr/Zr interface

In cold spray deposition, the adhesion of the sprayed particles that stack together to form the final coating is produced mostly by plastic deformation occurring upon impact on the substrate, in the particle being deposited and between sprayed particles. This process leaves a heavily deformed microstructure, with fine grain size and significant residual stresses [22], as displayed in Fig. 6a with an EBSD band contrast map from the Cr/Zr interfacial region of an as-fabricated sample. In the pristine sample, between the two materials, zirconium appears to have suffered a higher degree of plastic-deformation induced dynamic recrystallization which has left the material with 1-2 µm thick nanocrystalline layer and a 10-20 µm thick band with sub-micron grains (with no 2-5 µm grains). Beyond this layer, 2-5 µm sized grains start to appear as expected for the unaffected partially-recrystallized microstructure typical of the rod OPZ alloy [23–25]. As anticipated, the dynamically recrystallized region (studied in detail in [16]) can be divided into two different sub-bands. The first extends for a couple of microns from the Cr/Zr interface into the zirconium substrate. It is characterized by the smallest grains (tens of nanometres) and can be recognised in Fig. 6a as a black region with some small grey spots. The second sub-band comprises grains with a grain size between 100 nm and 1 µm. This band ends where the OPZ microstructure goes back to normal and the 2-5 µm sized grains appear. In the EBSD map presented in Fig. 6b, the microstructure of the same corresponding interfacial region is mapped for the autoclave exposed sample. Starting from the microstructure of the bulk OPZ, both sub-micron grains and 2-5 µm sized grains are found as expected for a partially recovered material, but the relative amount of grains appertaining to the two different families differs quite significantly between the as-fabricated and the exposed sample. In the as-fabricated material a larger portion of the mapped area is covered with fine grains, while for the exposed material most of the grains are 2-5 µm, or larger, in size. It is possible that this difference is caused by the autoclave exposure but it is important to keep in mind that a certain dispersion in the degree of recrystallization among as-fabricated claddings exists. Hence, it is difficult to associate with certainty the exposure at 415°C with the bulk recrystallization that seems to emerge, as seen in Fig. 6. With regard to the 1-2 µm nanocrystalline layer, this is detected in the exposed sample as well with some minor differences: immediately adjacent to the interface with chromium, grains seem to have grown slightly com-

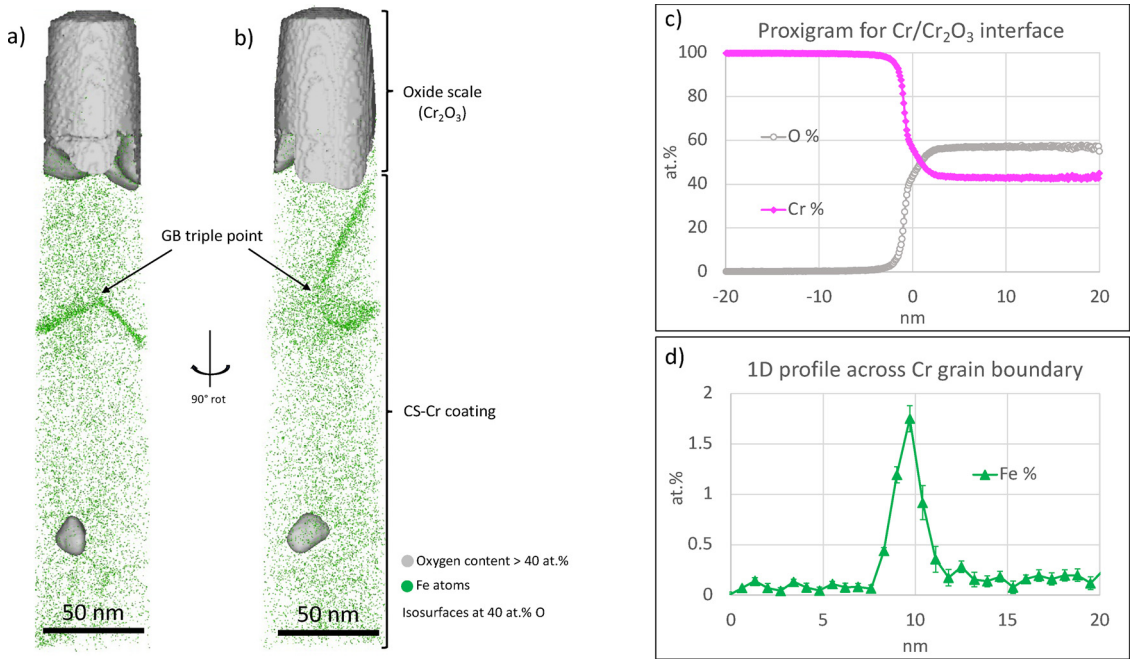

Fig. 5. (a) and (b) 3D reconstruction of APT data from the CS Cr-coating outer surface. Fe atoms in green, the grey surfaces represent chromium oxide (isosurfaces at 40 at.% O). (c) Proxigram displaying the composition profile across the Cr/Cr_2O_3 interface. (d) 1D concentration profile plot for Fe across the grain boundary of the CS-Cr coating. (For interpretation of the references to colour in this figure legend, the reader is referred to the web version of this article.)

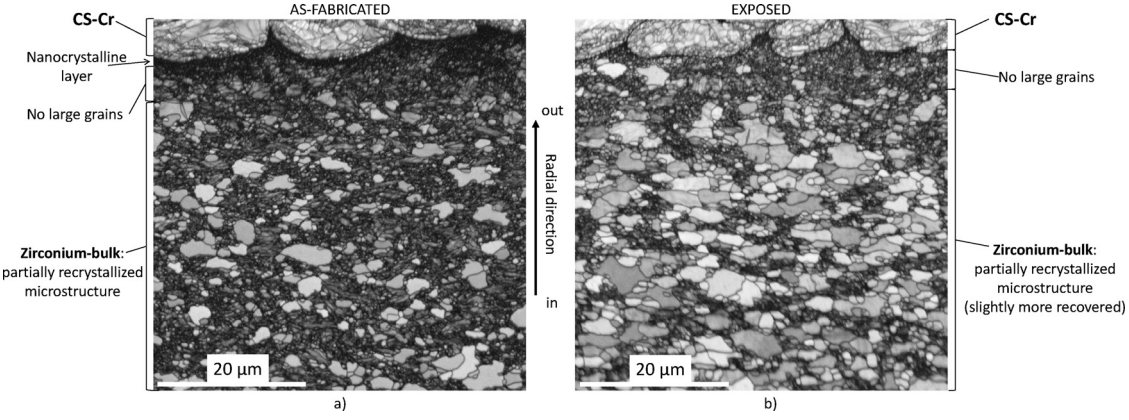

Fig. 6. EBSD maps over as-fabricated (a) and autoclave exposed (b) CS-Cr coated Optimized ZIRLO cladding cross-sections (Map size 50×50 µm).

pared with the as-fabricated material. Little or no difference is notable in the 10-20 µm thick band with sub-micron grains (with no 2-5 µm grains). On the Cr-side of the interface, the grain structure of the Cr-coating in the exposed sample looks slightly coarser. To evaluate if the differences noted in Fig. 6 between the as-fabricated and exposed materials are representative for the whole sample, a larger EBSD map was collected from both materials. The results are presented in Fig. 7. Here it is possible to see that there are clear fluctuations in the microstructure from region to region. Nevertheless, the main trends delineated previously are still valid: the recrystallization of the substrate appears mostly limited to the bulk; insignificant/slight grain coarsening can be seen in the region of the substrate within 10-20 µm from the coating, and the 1-2 µm nanocrystalline layer seems to recrystallize slightly. At this scale the presence of a 10-20 µm thick band of smaller grains, where no recrystallization has occurred, is even more clear.

Fig. 8 shows a comparison between bright-field TEM images of the as-fabricated and exposed materials where the interface between the Cr-coating and the Zr-substrate is analysed. Many dislocations and bend fringes are visible in both samples indicating heavy deformation. The size of Cr and Zr grains close to the interface is different in the two materials. The Cr-grains appear layered with orientation parallel to the interface in both samples but they are larger in the case of the exposed material. Due to their small size and the high degree of deformation they underwent, the Zr-grains are harder to unambiguously distinguish. Nonetheless, the grain structure appears coarser and more relaxed after exposure. The most important change that can be observed in the exposed sample is the presence of small particles and flake-like structures at the Cr/Zr interface itself. These particles are shown at higher magnification in box 1 in Fig. 8 and are a novelty, unreported for the as-fabricated material. Their presence is easier to detect in the Cr region because of the better contrast, but they can also be detected in a few places in the Zr where the grains have a lighter grey hue. To further understand these features, APT was employed. In Fig. 9, the compositions of the as-fabricated and exposed interfaces are compared. In the as-fabricated sample the intermixed bonding region (IBR) contains 60 at.% Zr and 30 at.% Cr, which corresponds to a metastable oversaturated solid solution of Cr in Zr. In the case of the exposed sample the proportion of Cr and Zr in

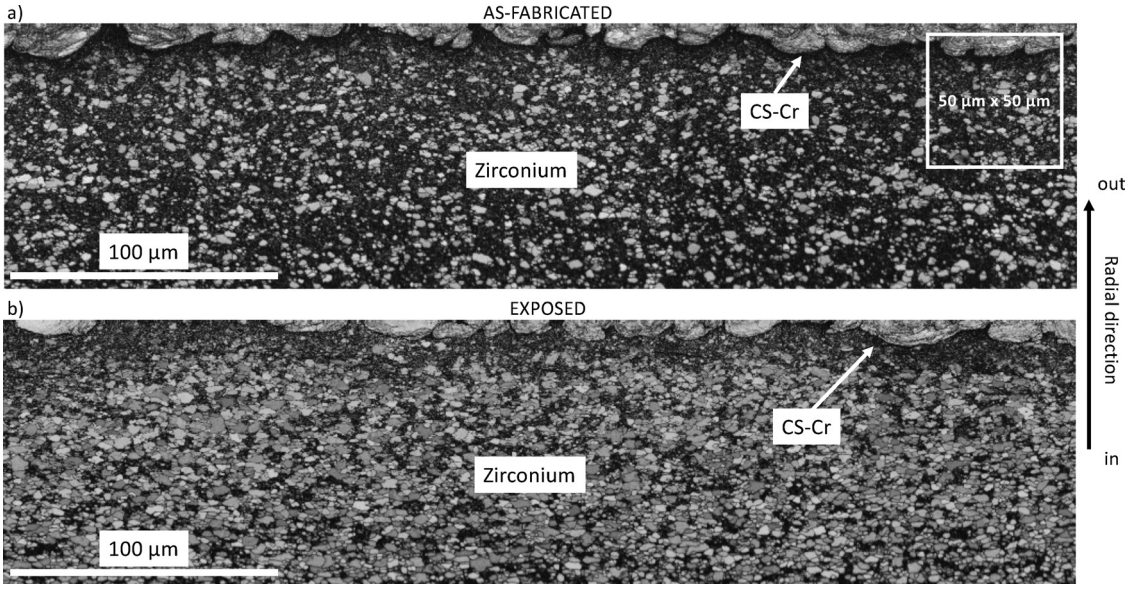

Fig. 7. EBSD maps over as-fabricated (a) and autoclave exposed (b) CS-Cr coated Optimized ZIRLO cladding cross-sections (Map size 400×100 µm).

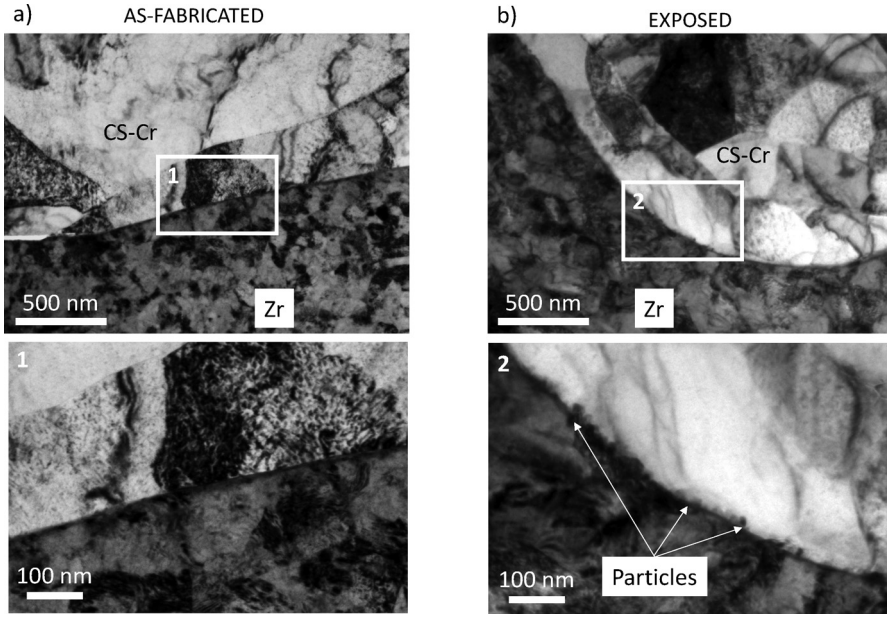

Fig. 8. BF-TEM imaging of Cr/Zr interface in CS-Cr coated Optimized ZIRLO claddings, respectively from as-fabbricated (a) and autoclave exposed (b) samples.

the IBR is different. It consists of 65 at.% Cr and 35 at.% Zr, which is much closer to the chemical composition of the $ZrCr_2$ Laves phase. In the as-fabricated material oxygen can be found mixed together with the Zr and Cr in the IBR, while in the exposed specimen the oxygen is found only outside the IBR on the Zr side. The solubility of oxygen in Zr is very high (up to 30 at.% in Zr at 415°C [26]), it is then reasonable to imagine the $ZrCr_2$ phase forming and pushing the O out to be dissolved in the Zr. This could explain the different O profiles around the Cr/Zr interface before and after the autoclave exposure. Further away from the interface into the substrate, a Zr-Cr-Fe phase is discovered (see Fig. 10). This phase has been found multiple times in the substrate at a distance of a few hundred nanometres from the interface, with chemical composition around 48 at.% Cr, 42 at.% Zr and 8 at. % Fe. The shape and distribution of this Zr-Cr-Fe phase seems to suggest that its nucleation and growth occurs along grain boundaries or dislocation walls. Moreover, this phase could be found exclusively near the Cr/Zr interface. In Fig. 11, APT reconstructions of different Zr grain boundaries at distances of 100 – 200 nm, 2.5 – 5 µm and 15 – 17.5 µm, respectively, from the interface are reported. This Zr-Cr-Fe phase is measured only at the grain boundaries closest to the Cr/Zr interface. Here, the Cr content reaches 40 at.% and Fe gets just above 6 at.%, while the grain boundaries further away from the Cr/Zr interface contain only Fe in modest amounts (0.3 – 0.7 at.%).

4. Discussion

4.1. Effective corrosion protection provided by the coating

The design concept behind the application of a metallic Cr coating on top of the Zr-alloy is to obtain a passivating scale of chromia [2]. The Cr_2O_3 layer should form on the surface of the coating and it should be dense, adherent and impermeable to the diffu-

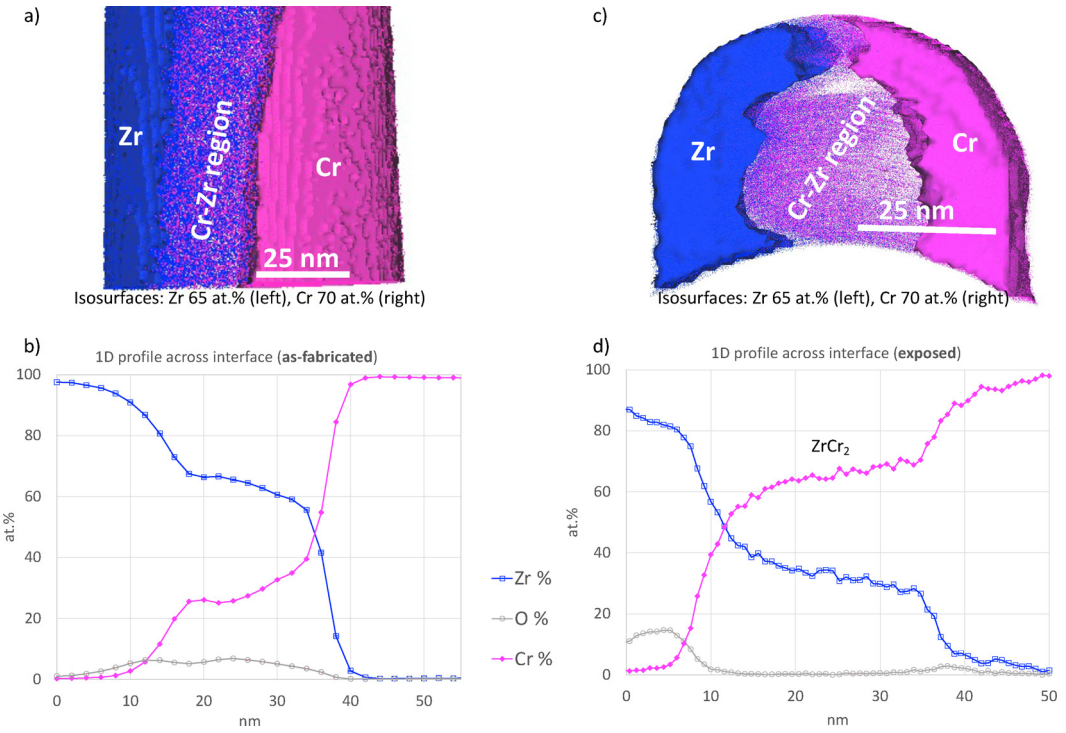

Fig. 9. 3D reconstruction of APT data from the Cr/Zr interface in CS Cr-coated Optimized ZIRLO claddings. Cr atoms in magenta, Zr atoms in blue. The blue surface represent the Zr-substrate, the pink surface represent the Cr-coating. (a) 3D reconstruction of as-fabricated sample. (b) 1D composition profile across Cr/Zr interface of as-fabricated material. (c) 3D reconstruction of autoclave exposed sample. (d) 1D composition profile across Cr/Zr interface of autoclave exposed material. (For interpretation of the references to colour in this figure legend, the reader is referred to the web version of this article.)

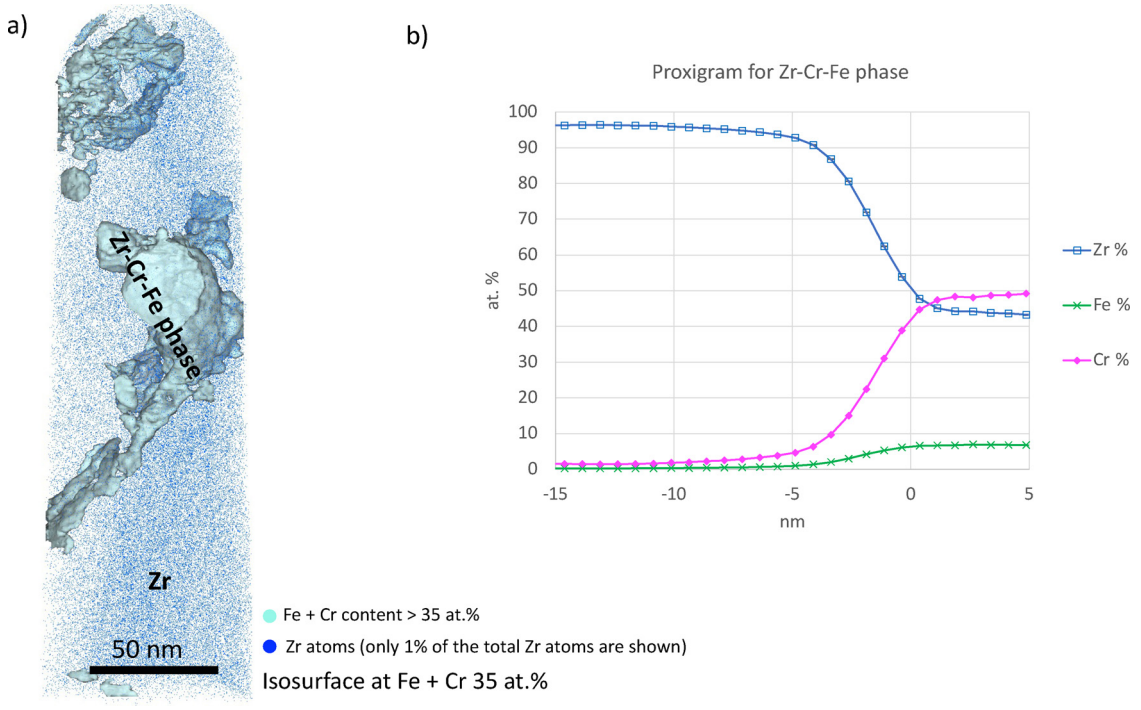

Fig. 10. (a) 3D reconstruction of APT data from the Zr-substrate, 100-200 nm distance from the Cr/Zr interface. Zr atoms in blue (only 1% shown). Light blue surface encloses a Zr-Cr-Fe phase (isosurface set at Fe+Cr content at 35 at.%). (b) Proxigram across Zr-Cr-Fe phase isosurface. (For interpretation of the references to colour in this figure legend, the reader is referred to the web version of this article.)

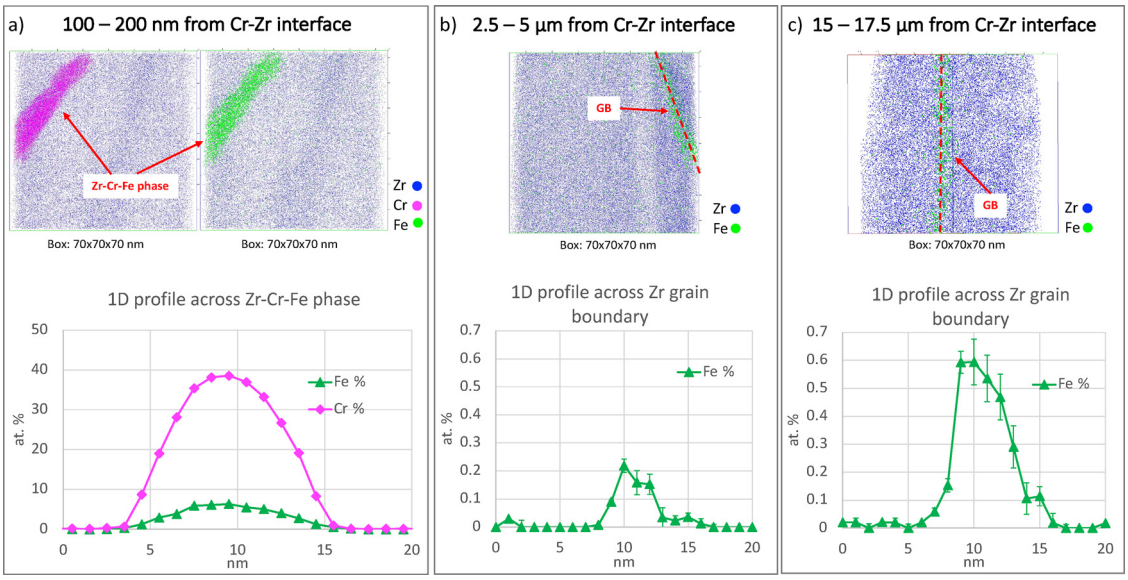

Fig. 11. 3D reconstruction of APT data for grain boundaries extracted from the autoclave exposed Zr-substrate respectively at 100 – 200 nm (a), 2.5 – 5 µm (b) and 15 – 17.5 µm (c) distance from the Cr/Zr interface coupled with the corresponding 1D concentration profile plots for Fe and Cr (when present) across the grain boundary. Zr atoms in blue (only 5% shown), Cr atoms in pink, Fe atoms in green. (For interpretation of the references to colour in this figure legend, the reader is referred to the web version of this article.)

sion of oxygen. Chromia can be dissolved in water and the rate at which it dissolves depends on water chemistry, partial pressure of oxygen and suchlike. Hence, chromia is predicted to form on the surface of the Cr-coating and it is expected to start to slowly dissolve into the water. The growth rate of the oxide scale, which depends on the diffusion of oxygen through it, together with the rate at which the chromia is dissolved into water determine the equilibrium thickness of the obtained chromia scale and consequently the rate at which the metal is corroded away [27]. As observed in Fig. 3, an 80-100 nm thick, dense layer of oxide is found with TEM on the surface of the Cr-coating. This is a significant improvement in oxidation resistance when compared with uncoated Zr-claddings that develop ZrO_2 scales with thicknesses in the few-microns range for exposures under similar PWR conditions [28,29]. When compared with other Cr-coatings exposed to similar conditions, all Cr-coatings end up forming a 50-100 nm thick chromia scale [17,30,31]. Additionally, from the SEM analysis of the cladding cross-sections in Fig. 1, the corrosion of the coating upon autoclave exposure appears to be negligible. Overall, the formed oxide can be deemed protective and stable. APT measurements confirmed the composition of this oxide layer to be around 40 at.% Cr and 60 at.% O, corresponding to chromia (Cr_2O_3). The composition of the oxide is uniform across its thickness and no segregation of other elements is observed. The interface between the oxide scale and the Cr-coating is characterized by areas of intimate contact, but also areas containing small voids, suggesting an outward growth mechanism for the oxide. Chromia starts nucleating on the outer surface of the coating, O atoms are provided by the autoclave environment while Cr atoms from the coating diffuse to the outer chromia surface, leaving the metal surface (which equates to an injection of vacancies into the coating surface). The vacancies tend to coalesce and small voids are formed at the oxide/metal interface. With enough time and higher temperatures, diffusion of Cr atoms from the bulk of the coating would fill-in the voids. Due to the relatively low temperature of the exposure, the voids at the oxide/metal interface have yet to be filled as is common for oxidation under similar conditions [18,32]. Small oxide particles seem to be distributed in the metallic Cr in a band 200 nm thick. These particles could not be found in the as-fabricated material so their formation must have occurred during the autoclave exposure. These oxide particles found underneath the surface could be explained by the oxidation of nanometric porosities left behind by the outward diffusion of Cr atoms during the formation of the chromia scale [32,33]. As demonstrated by Fig. 2b, the ability to effectively protect the substrate from oxidation is not compromised even when the coating is breached. From an industrial point of view, guaranteeing the perfect integrity of a few micron thick coating over thousands of cladding tubes is extremely challenging. Additionally, transport and in-reactor degradation mechanisms as debris fretting could result in the opening of a gap in the coating. Seeing that, even when damaged, the coating is able to provide protection to the substrate is of great significance. When part of the Zr is exposed, oxidation is limited to the region immediately underneath the coating gap. Moreover, no further degradation or spallation seems to be initiated by the formation of a breach in the coating, which offers a significant margin of protection even if damages to the coating were to arise due to debris fretting or other in reactor deterioration phenomena [4].

4.2. Microstructural evolution of the Cr/Zr interface

4.2.1. Diffusion during exposure in autoclave

During the autoclave exposure a certain degree of diffusion in the investigated material system is expected to occur. The volume diffusion coefficients at 415°C for Fe, Cr and Zr (self-diffusion) in α-Zr are approximately $D_v^{Fe} \approx 1.4 \cdot 10^{-12}\ m^2 s^{-1}$, $D_v^{Cr} \approx 1.6 \cdot 10^{-17}\ m^2 s^{-1}$ and $D_v^{Zr} \approx 1 \cdot 10^{-26}\ m^2 s^{-1}$ [34]. Over a period of 90 days, these values would provide the following diffusion lengths: $\sqrt[2]{D_v^{Fe} * t} \approx 3.3\ mm$, $\sqrt[2]{D_v^{Cr} * t} \approx 11.3\ \mu m$ and $\sqrt[2]{D_v^{Zr} * t} \approx 2.8$ Å. Including grain boundary diffusion into the rough evaluation of the diffusivities is somehow difficult. The presence of a nanocrystalline layer in the Zr substrate adjacent to the Cr/Zr interface and the fine grains that can be found in the partially recrystallized microstructure of the OPZ alloy (both shown in Fig. 6) provide an elevated density of grain boundaries, which could further increase the overall values for the calculated diffusivities. In the studied temperature range, grain boundary diffusion could even be the dominant diffusive phenomena, potentially increasing the cal-

culated diffusivities by 2-5 orders of magnitude [35–37]. In addition, diffusion processes are not isotropic in the hexagonal close-packed crystalline structure of α-Zr. In fact, diffusivity parallel to the c-direction is generally 3-5 times larger than diffusivity perpendicular to the c-direction. Though, since the diffusivities for the elements taken into consideration differ already by many orders of magnitude, this anisotropy can be assumed negligible for the general discussion. Overall, during the studied autoclave exposures, interstitial diffusing elements as Fe had the chance to move quite freely in the zirconium substrate and can be assumed to have reached the most energetically favourable configuration. Cr, characterised by a mixed diffusion mechanism, has a significantly lower diffusion rate, but considering the calculated bulk diffusion length of around 10 µm, plus the proximity of the Zr nanocrystalline layer with the Cr/Zr interface, it would be reasonable to assume that Cr from the coating could penetrate into the Zr substrate for about 10-20 µm. On the other hand, the diffusion length of Zr atoms is shorter than a unit cell so that Zr has to be considered practically frozen into place. Even considering grain boundary diffusion it is difficult to imagine long-range diffusion of Zr at this temperature. As a result, Zr diffusion would represent the main limiting factor for any diffusive processes such as phase nucleation or transformation.

The high mobility of Fe would explain how the measured Zr-Cr-Fe phase has formed. The Fe content in the OPZ is relatively low at around 0.4 at.%, and most of it is normally tied in secondary phase particles (SPPs) rather than being distributed in the matrix. Generally, SPPs are not expected to dissolve at operating temperature. The exposure to operating temperature in autoclave can trigger the movement of the Fe from the SPPs but with no other modification of the system, the diffusing Fe atoms would be captured again by another SPP. As shown in the previous work [16], in as-fabricated CS-Cr coated OPZ claddings, small amounts of Cr from the CS coating were found diffusing along grain boundaries into the OPZ substrate for distances of about 100-200 nm. The presence of this Cr, segregated along grain boundaries in the substrate adjacent to the coating, plus the high density of grain boundaries due to the presence of a nanocrystalline layer in the same region, could have produced a network of surfaces able to capture the diffusing Fe atoms. In conclusion, the diffusion of Cr into the substrate during deposition of the coating, additional diffusion of Cr into the substrate during autoclave exposure, and the exceptional freedom of movement for the Fe atoms in Zr during autoclave need to be considered in order to explain the formation of the Zr-Cr-Fe phase. The main consequence of this phenomenon on the cladding material could be a slow size reduction of the Fe-rich SPPs used in the OPZ alloy to improve mechanical properties. The slow dissolution of the SPPs would go in favour of the formation of a network of Zr-Cr-Fe phase nucleating and growing approximately in the same regions where Cr from the coating manage to reach. Despite the calculated Cr diffusion length of about 8 µm, Cr and the Zr-Cr-Fe phase could be found exclusively at Zr grain boundaries adjacent to the Cr/Zr interface (100 – 200 nm distance). Grain boundaries further away contained only small amounts of Fe and no Cr at all, similar to grain boundaries of as-fabricated OPZ. This result suggests that, despite the theoretical possibility of Cr diffusion into the substrate, all the diffusing Cr reacts with Zr forming nuclei of $ZrCr_2$ Laves phase at the very Cr/Zr interface or reacts with Fe and Zr at the grain boundaries near the Cr/Zr interface forming the Zr-Cr-Fe phase. In both cases, it seems like Cr does not manage to penetrate the substrate beyond the 100 – 200 nm depth.

4.2.2. Thermal recrystallization

Recrystallization in OPZ is usually not expected for temperatures around the operating condition. The autoclave testing was performed at 415°C, higher than the actual PWR operating temperature of around 325°C. The higher temperature is meant to speed up all oxidation and diffusive processes so as to simulate the equivalent of longer times at actual operating temperature, but it could also have triggered recrystallization in OPZ cladding. Recrystallization is a thermally activated process [38,39] and if the threshold temperature lays in the 325-415°C range, recrystallization would become visible in the autoclave tested material while still not being possible during operation. The heat treatments generally used on OPZ claddings in the final step of production are the following: (a) stress relieve annealing (2h at 465°C), (b) partial recrystallization (2h at 500°C), or (c) recrystallization (2.5h at 595°C) [25,40]. It is possible then, that 90 days at 415°C could have produced the degree of recrystallization measured in the bulk of the exposed OPZ cladding as if it was a lower temperature, longer time heat treatment [41], rendering this phenomenon not too relevant for the real case scenario. What makes this result interesting, though, is the comparison with the 10-20 µm region where almost no recrystallization has taken place instead. The driving force behind recrystallization is the stored energy from deformation. An heavily deformed material will tend to evolve towards a more relieved microstructure by creating new stress-free zones through recrystallization. Surface energy can also play a role, many small grains have much higher surface density than few large grains. Larger grains are energetically favourable and, if allowed, a nanocrystalline system will tend towards larger grains. For these reasons, because the nanocrystalline region produced by the application of the CS coating suffered higher degrees of deformation, it should have experienced the largest amount of recrystallization. In the presented experiments the opposite seems to happen. In the bulk of the substrate, far from the Cr/Zr interface, large grains grow at the expense of smaller ones through Ostwald ripening [42,43]. While in the nanocrystalline layer and in the 10-20 µm region depleted of large grains, not much recrystallization could be seen. Competition between grains of similar size could be creating a metastable equilibrium that might explain the relatively low degree of recrystallization seen in this region [44].

4.2.3. Chemical evolution of the intermixed bonding region

Cr and Zr can form the intermetallic Laves phase $ZrCr_2$. The formation of such phase has been repeatedly reported for high temperature exposed Cr-coated zirconium claddings [9,17,45] and does not surprise when temperatures in the range of 800-1200°C are involved. What is interesting about the results shown in Fig. 8 and Fig. 9 is that nucleation of this phase looks possible even at 415°C. As is possible to see in Fig. 8b, small particles of Laves phase can be found uniformly distributed along the Cr/Zr interface, which would suggest that is a wide spread event. The presence of nuclei of this phase reduces the energy barrier for further growth of the intermetallic phase. The growth of this phase could potentially be possible even during operation causing gradual changes in the nature of the IBR and in the Cr/Zr interface properties. The limiting factor for the growth of this phase would mostly be the diffusion of Zr. Even if Cr could potentially reach the interface quite easily to drive growth, diffusion of Zr at PWR operating temperature is almost none, which strongly limits the allowed growth rate of this phase. For the same reason, almost no diffusion of Zr into the Cr-coating is measured. $ZrCr_2$ is a brittle phase and its presence could potentially cause an embrittlement of the Cr/Zr interface. Nonetheless, no spallation of the coating or significant embrittlement of the Cr/Zr interface is reported for exposures at higher temperature [9,17,45]. In these conditions the $ZrCr_2$ layer can grow to thicknesses of a few microns but it seems to produce no significant effects on the Cr/Zr interface properties beyond local increase in hardness. Hence, the effects of a few nuclei (50 nm in diameter) sparsely distributed along the Cr/Zr interface should not produce significant changes in the interface properties. Irradiation

could have two opposite effects on these particles. Irradiation is known to dissolve the Laves phase SPPs that are distributed by design in the matrix of many Zr-alloys. On the other hand, irradiation promotes diffusion and could speed up the Laves phase nucleation and growth process at the Cr/Zr interface [46–48]. In order to determine which of the two phenomena would prevail under irradiation, an in-depth study of irradiated material is needed.

5. Conclusions

The studied CS-Cr coating has provided good protection from water oxidation at 415°C over a period of 90 days in PWR water chemistry. The resulting oxide scale is composed of chromia and its thickness ranges between 80 nm and 100 nm. Even where the substrate is partially exposed to water due to the presence of a gap in the coating, no spallation or other detrimental effect on the overall cladding or coating occur. $ZrCr_2$ Laves phase is reported to nucleate sparsely in the intermixed bonding region that is found at the Cr/Zr interface. This can be considered a consequence of the autoclave exposure. The presence of these nuclei (less than 50 nm in size) reduces the energy barrier for the formation and growth of $ZrCr_2$ at the interface, still diffusion of Zr remains the main limiting factor. Thermal recrystallization has taken place in the exposed material. The 1-2µm nanocrystalline layer has coarsened slightly and a small degree of recrystallization has been observed in the region of the substrate adjacent to the coating (10-20 µm distance from the coating). The competition between small grains of similar sizes is deemed responsible for the lack of recrystallization in this region. Recrystallization in the coating and at the coating/substrate interface could be beneficial because of the improvement provided to the ductility of the coating, but the changes in the microstructure that occurred during autoclave exposure are probably too small to produce a significant change in mechanical properties. Overall, only very small changes are observed in the coated cladding chemistry and microstructure after exposure to simulated operating conditions. This, combined with the provided improvement in corrosion resistance, indicate that Cr-coated claddings are well suited for operation under normal PWR conditions. Characterization of material exposed at similar temperature for longer times could shed some light on the kinetics of the different phenomena observed. Moreover, detailed studies of Cr-coated zirconium claddings exposed to simulated accident conditions are crucial in assessing the extent of protectiveness offered by the Cr-coating in a severe accident scenario.

Declaration of Competing Interest

The authors declare that they have no known competing financial interests or personal relationships that could have appeared to influence the work reported in this paper.

CRediT authorship contribution statement

Andrea Fazi: Investigation, Writing – original draft, Visualization, Conceptualization. **Krystyna Stiller:** Writing – review & editing, Conceptualization. **Hans-Olof Andrén:** Writing – review & editing, Conceptualization. **Mattias Thuvander:** Supervision, Project administration, Funding acquisition, Writing – review & editing, Conceptualization.

Acknowledgements

This project is financially supported by the Swedish Foundation for Strategic Research (SSF) (Grant number: EM16-0031). Westinghouse Electric Sweden is acknowledged for providing the analysed material. All the experimental work presented in this paper was performed at Chalmers Materials Analysis Laboratory (CMAL).

References

[1] S.J. Zinkle, K.A. Terrani, J.C. Gehin, L.J. Ott, L.L. Snead, Accident tolerant fuels for LWRs: A perspective, J. Nucl. Mater. 448 (2014) 374–379, doi:10.1016/j.jnucmat.2013.12.005.
[2] K.A. Terrani, Accident tolerant fuel cladding development: Promise, status, and challenges, J. Nucl. Mater. 501 (2018) 13–30, doi:10.1016/j.jnucmat.2017.12.043.
[3] R.V. Umretiya, B. Elward, D. Lee, M. Anderson, R.B. Rebak, J.V. Rojas, Mechanical and chemical properties of PVD and cold spray Cr-coatings on Zircaloy-4, J. Nucl. Mater. 541 (2020) 152420, doi:10.1016/j.jnucmat.2020.152420.
[4] IAEA, TECDOC-709: Fuel failure in normal operation of water reactors: experience, mechanisms and management, 1993.
[5] H. Yeom, K. Sridharan, Cold spray technology in nuclear energy applications: A review of recent advances, Ann. Nucl. Energy. 150 (2021) 107835, doi:10.1016/j.anucene.2020.107835.
[6] P. Cavaliere, Cold-Spray Coatings: Recent Trends and Future perspectives, Springer, 2017, doi:10.1007/978-3-319-67183-3.
[7] J.C. Brachet, M.Le Saux, M.Le Flem, S. Urvoy, E. Rouesne, T. Guilbert, C. Cobac, F. Lahogue, J. Rousselot, M. Tupin, P. Billaud, C. Hossepied, F. Schuster, F. Lomello, A. Billard, G. Velisa, E. Monsifrot, J. Bischoff, A. Ambard, in: On-going studies at CEA on chromium coated zirconium based nuclear fuel claddings for enhanced Accident Tolerant LWRs Fuel, TopFuel, 2015, pp. 31–38.
[8] B. Maier, H. Yeom, G. Johnson, T. Dabney, J. Walters, P. Xu, J. Romero, H. Shah, K. Sridharan, Development of cold spray chromium coatings for improved accident tolerant zirconium-alloy cladding, J. Nucl. Mater. 519 (2019) 247–254, doi:10.1016/j.jnucmat.2019.03.039.
[9] H. Yeom, B. Maier, G. Johnson, T. Dabney, M. Lenling, K. Sridharan, High temperature oxidation and microstructural evolution of cold spray chromium coatings on Zircaloy-4 in steam environments, J. Nucl. Mater. 526 (2019) 151737, doi:10.1016/j.jnucmat.2019.151737.
[10] H.-G. Kim, I.-H. Kim, Y.-I. Jung, D.-J. Park, J.-H. Park, B.-K. Choi, Y.-H. Lee, Out-of-pile performance of surface-modified Zr cladding for accident tolerant fuel in LWRs, J. Nucl. Mater. 510 (2018) 93–99, doi:10.1016/j.jnucmat.2018.07.061.
[11] M. Ševeček, A. Gurgen, A. Seshadri, Y. Che, M. Wagih, B. Phillips, V. Champagne, K. Shirvan, Development of Cr cold spray–coated fuel cladding with enhanced accident tolerance, Nucl. Eng. Technol. 50 (2018) 229–236, doi:10.1016/j.net.2017.12.011.
[12] M. Wagih, B. Spencer, J. Hales, K. Shirvan, Fuel performance of chromium-coated zirconium alloy and silicon carbide accident tolerant fuel claddings, Ann. Nucl. Energy. 120 (2018) 304–318, doi:10.1016/j.anucene.2018.06.001.
[13] A. G2-88(2002), Standard Test Method for Corrosion Testing of Products of Zirconium, Hafnium, and Their Alloys in Water at 680°F or in Steam at 750°F, 88 (1988) 1–8. https://doi.org/10.1520/G0002-88R02.
[14] K. Thompson, D. Lawrence, D.J. Larson, J.D. Olson, T.F. Kelly, B. Gorman, In situ site-specific specimen preparation for atom probe tomography, Ultramicroscopy 107 (2007) 131–139, doi:10.1016/j.ultramic.2006.06.008.
[15] R.M. Langford, M. Rogers, In situ lift-out: Steps to improve yield and a comparison with other FIB TEM sample preparation techniques, Micron 39 (2008) 1325–1330, doi:10.1016/j.micron.2008.02.006.
[16] A. Fazi, H. Aboulfadl, A.H.S. Iyer, M. Sattari, K.M. Stiller, P. Lokhande, M. Thuvander, H.O. Andren, Characterization of as-deposited cold sprayed Cr-coating on Optimized ZIRLO™ claddings, J. Nucl. Mater. 549 (2021) 152892, doi:10.1016/j.jnucmat.2021.152892.
[17] J.C. Brachet, I. Idarraga-Trujillo, M.Le Flem, M.Le Saux, V. Vandenberghe, S. Urvoy, E. Rouesne, T. Guilbert, C. Toffolon-Masclet, M. Tupin, C. Phalippou, F. Lomello, F. Schuster, A. Billard, G. Velisa, C. Ducros, F. Sanchette, Early studies on Cr-Coated Zircaloy-4 as enhanced accident tolerant nuclear fuel claddings for light water reactors, J. Nucl. Mater. 517 (2019) 268–285, doi:10.1016/j.jnucmat.2019.02.018.
[18] R.B. Rebak, M. Larsen, Y.-J. Kim, Characterization of oxides formed on iron-chromium-aluminum alloy in simulated light water reactor environments, Corros. Rev. 35 (2017) 177–188, doi:10.1515/corrrev-2017-0011.
[19] T. Dabney, G. Johnson, H. Yeom, B. Maier, J. Walters, K. Sridharan, Experimental evaluation of cold spray FeCrAl alloys coated zirconium-alloy for potential accident tolerant fuel cladding, Nucl. Mater. Energy. 21 (2019) 100715, doi:10.1016/j.nme.2019.100715.
[20] B. Gault, M.P. Moody, J.M. Cairney, S.P. Ringer, in: Atom Probe Microscopy and Materials Science, Springer New York, New York, NY, 2012, pp. 299–311, doi:10.1007/978-1-4614-3436-8_9.
[21] B. Gault, M.P. Moody, J.M. Cairney, S.P. Ringer, Analysis Techniques for Atom Probe Tomography, in: Atom Probe Microsc., Springer New York, New York, NY, 2012: pp. 213–297. https://doi.org/10.1007/978-1-4614-3436-8_8.
[22] C. Lee, J. Kim, Microstructure of Kinetic Spray Coatings: A Review, J. Therm. Spray Technol. 24 (2015) 592–610, doi:10.1007/s11666-015-0223-5.
[23] K.L. Murty, I. Charit, Texture development and anisotropic deformation of zircaloys, Prog. Nucl. Energy. 48 (2006) 325–359, doi:10.1016/j.pnucene.2005.09.011.
[24] G. Sabol, ZIRLO™ — An Alloy Development Success, J. ASTM Int. 2 (2005) 12942, doi:10.1520/JAI12942.
[25] J.P. Foster, H.K. Yueh, R.J. Comstock, M. Limback, B. Kammenzind, S.W. Dean, ZIRLO™ Cladding Improvement, J. ASTM Int. 5 (2008) 101188, doi:10.1520/JAI101188.
[26] N.B. Lazar Rokhlin, Tatiana Dobatkina, Natalia Kolchugina, Oleksandr Dovbenko, M. Materials Science International Team, Phase diagram of the O-Zr binary system: Datasheet from MSI Eureka in SpringerMa-

terials, (2016). https://materials.springer.com/msi/phase-diagram/docs/sm_msi_r_10_010853_01_full_LnkDia1.
[27] N.K. Othman, N. Othman, J. Zhang, D.J. Young, Effects of water vapour on isothermal oxidation of chromia-forming alloys in Ar/O2 and Ar/H2 atmospheres, Corros. Sci. 51 (2009) 3039–3049, doi:10.1016/j.corsci.2009.08.032.
[28] A.T. Motta, A. Couet, R.J. Comstock, Corrosion of Zirconium Alloys Used for Nuclear Fuel Cladding, Annu. Rev. Mater. Res. 45 (2015) 311–343, doi:10.1146/annurev-matsci-070214-020951.
[29] G. Sabol, R. Comstock, R. Weiner, P. Larouere, R. Stanutz, In-Reactor Corrosion Performance of ZIRLO™ and Zircaloy-4, in: Zircon, Nucl. Ind. Tenth Int. Symp. (2009) ASTM International, 100 Barr Harbor Drive, PO Box C700, West Conshohocken, PA 19428-2959pp. 724-724–21, doi:10.1520/STP15217S.
[30] C. Tang, M. Stueber, H.J. Seifert, M. Steinbrueck, Protective coatings on zirconium-based alloys as accident-Tolerant fuel (ATF) claddings, Corros. Rev. 35 (2017) 141–165, doi:10.1515/corrrev-2017-0010.
[31] B. Maier, H. Yeom, G. Johnson, T. Dabney, J. Walters, P. Xu, J. Romero, H. Shah, K. Sridharan, Development of cold spray chromium coatings for improved accident tolerant zirconium-alloy cladding, J. Nucl. Mater. 519 (2019) 247–254, doi:10.1016/j.jnucmat.2019.03.039.
[32] S. Henry, J. Mougin, Y. Wouters, J.P. Petit, A. Galerie, Characterization of chromia scales grown on pure chromium in different oxidizing atmospheres, Mater. High Temp. 17 (2000) 231–234, doi:10.1179/mht.2000.17.2.008.
[33] M. Metikoš-Huković, M. Ceraj-Cerić, p-Type and n-Type Behavior of Chromium Oxide as a Function of the Applied Potential, J. Electrochem. Soc. 134 (1987) 2193–2197, doi:10.1149/1.2100850.
[34] G.M. Hood, Point defect diffusion in α-Zr, J. Nucl. Mater. 159 (1988) 149–175, doi:10.1016/0022-3115(88)90091-8.
[35] K. Vieregge, C. Herzig, Grain boundary diffusion in α-zirconium. Part I: Self-diffusion, J. Nucl. Mater. 173 (1990) 118–129, doi:10.1016/0022-3115(90)90250-Q.
[36] K. Vieregge, C. Herzig, Grain boundary diffusion in α-zirconium. Part II: Fast diffusing cobalt bulk interstitials, J. Nucl. Mater. 175 (1990) 29–41, doi:10.1016/0022-3115(90)90266-P.
[37] P. Tejland, H.O. Andrén, G. Sundell, M. Thuvander, B. Josefsson, L. Hallstadius, M. Ivermark, M. Dahlbäck, Oxidation mechanism in zircaloy-2 - The effect of SPP size distribution, ASTM Spec. Tech. Publ. (2015) 373–403, doi:10.1520/STP154320130052.
[38] E. Calla, D.G. McCartney, P.H. Shipway, Effect of Deposition Conditions on the Properties and Annealing Behavior of Cold-Sprayed Copper, J. Therm. Spray Technol. 15 (2006) 255–262, doi:10.1361/105996306X108192.
[39] V.D. Hiwarkar, S.K. Sahoo, I. Samajdar, K. Narasimhan, K.V. Mani Krishna, G.K. Dey, D. Srivastava, R. Tewari, S. Banerjee, Annealing of cold worked two-phase Zr-2.5 Nb-Associated microstructural developments, J. Nucl. Mater. 384 (2009) 30–37, doi:10.1016/j.jnucmat.2008.10.006.
[40] J.P. Foster, S.A. Worcester, R.J. Comstock, P. Township, W. County, P. Assignee, Processing zirconium alloy used in light water reactors for specified creep rate, US5125985A, 1992. https://patentimages.storage.googleapis.com/3b/31/b2/4c17c039cfa196/US5125985.pdf.
[41] J.W.C. Dunlop, Y.J.M. Bréchet, L. Legras, H.S. Zurob, Modelling isothermal and non-isothermal recrystallisation kinetics: Application to Zircaloy-4, J. Nucl. Mater. 366 (2007) 178–186, doi:10.1016/j.jnucmat.2006.12.074.
[42] K. Onel, J. Nutting, Recrystallization and grain growth in deformed and tempered carbon steels, Met. Sci. 15 (1981) 89–94, doi:10.1179/030634581790426624.
[43] X. dong Huo, X. ping Mao, S. xia Lü, Effect of annealing temperature on recrystallization behavior of cold rolled ti-microalloyed steel, J. Iron Steel Res. Int. 20 (2013) 105–110, doi:10.1016/S1006-706X(13)60164-8.
[44] M. Saber, C.C. Koch, R.O. Scattergood, Thermodynamic grain size stabilization models: An overview, Mater. Res. Lett. 3 (2015) 65–75, doi:10.1080/21663831.2014.997894.
[45] J.C. Brachet, E. Rouesne, J. Ribis, T. Guilbert, S. Urvoy, G. Nony, C. Toffolon-Masclet, M.Le Saux, N. Chaabane, H. Palancher, A. David, J. Bischoff, J. Augereau, E. Pouillier, High temperature steam oxidation of chromium-coated zirconium-based alloys: Kinetics and process, Corros. Sci. 167 (2020) 108537, doi:10.1016/j.corsci.2020.108537.
[46] A. Harte, M. Topping, P. Frankel, D. Jädernäs, J. Romero, L. Hallstadius, E.C. Darby, M. Preuss, Nano-scale chemical evolution in a proton-and neutron-irradiated Zr alloy, J. Nucl. Mater. 487 (2017) 30–42, doi:10.1016/j.jnucmat.2017.01.049.
[47] G. Sundell, M. Thuvander, P. Tejland, M. Dahlbäck, L. Hallstadius, H.-O. Andrén, Redistribution of alloying elements in Zircaloy-2 after in-reactor exposure, J. Nucl. Mater. 454 (2014) 178–185, doi:10.1016/j.jnucmat.2014.07.072.
[48] J. Eriksson, G. Sundell, P. Tejland, H.-O. Andrén, M. Thuvander, An atom probe tomography study of the chemistry of radiation-induced dislocation loops in Zircaloy-2 exposed to boiling water reactor operation, J. Nucl. Mater. 550 (2021) 152923, doi:10.1016/j.jnucmat.2021.152923.